Topologically protected magnetoelectric switching in a multiferroic

Louis Ponet,[1,2,3] S. Artyukhin,[1] Th. Kain,[4] J. Wettstein,[4] Anna Pimenov,[4] A. Shuvaev,[4] X. Wang,[5,6] S.-W. Cheong,[6] Maxim Mostovoy,[7] and Andrei Pimenov[4]

[1] *Quantum Materials Theory, Istituto Italiano di Tecnologia, 16163 Genova, Italy*
[2] *Scuola Normale Superiore di Pisa, 56126 Pisa, Italy*
[3] *presently at École Polytechnique Fédérale de Lausanne, 1015 Lausanne, Switzerland*
[4] *Institute of Solid State Physics, Vienna University of Technology, 1040 Vienna, Austria*
[5] *School of Aerospace Engineering, Beijing Institute of Technology, Beijing, 100081, China*
[6] *Rutgers Center for Emergent Materials and Department of Physics and Astronomy, Rutgers University, New Jersey 08854, USA*
[7] *Zernike Institute for Advanced Materials, University of Groningen, the Netherlands.*

(Dated: January 23, 2023)

Electric control of magnetism and magnetic control of ferroelectricity can improve energy efficiency of magnetic memory and data processing devices [1]. However, the necessary magnetoelectric switching is hard to achieve, and requires more than just a coupling between spin and charge degrees of freedom [2–5]. We show that an application and subsequent removal of a magnetic field reverses the electric polarization of the multiferroic $GdMn_2O_5$, thus requiring two cycles to bring the system back to the original configuration. During this unusual hysteresis loop, four states with different magnetic configurations are visited by the system, with one half of all spins undergoing unidirectional full-circle rotation in increments of $\sim 90°$. Therefore, $GdMn_2O_5$ acts as a magnetic crankshaft converting the back-and-forth variations of the magnetic field into a circular spin motion. This peculiar four-state magnetoelectric switching emerges as a topologically protected boundary between different two-state switching regimes. Our findings establish a paradigm of topologically protected switching phenomena in ferroic materials.

Introduction – The holy grail of permanent storage technology is the control of stable robust states in the storage medium by efficient means [6–8]. Magnetoelectric and multiferroic materials offer a promising avenue for manipulation of digital information by leveraging the cross-coupling between ferroelectric and magnetic orders [1]. Recent advances in the field of multiferroics led to a deeper understanding of microscopic mechanisms for the magnetoelectric coupling [9–13]. At the same time, magnetoelectric switching, allowing to reverse the magnetization direction with an electric field or to flip the electric polarization with an applied magnetic field, is much less understood and is difficult to realize due to different symmetry properties of the ferroelectric and magnetic orders [1–5]. The simplest magnetoelectric effect occurs in materials such as Cr_2O_3, where the magnetization and electric polarization are linearly coupled by an antiferromagnetic spin ordering that breaks both time reversal and inversion symmetries[14]. More complex magnetoelectric switching occurs in e.g. multiferroic rare-earth orthoferrites with composite domain walls that are both ferroelectric and ferromagnetic [15, 16].

Here, we report the discovery of a novel magnetoelectric switching behavior that depends on the magnetic field orientation. This leads to three distinct switching regimes, where the middle one showcases a novel topologically protected behavior where the system switches unidirectionally between four magnetic configurations (referred to as states, two at low fields and two at high fields) when the field is swept up and down twice. Half of the spins perform a full 360° unidirectional rotation in approximately 90° increments during the field sweeps, while the polarization is reversed twice. This represents a microscopic analogue of a crankshaft, converting linear changes of the field into a rotational motion of spins. It also acts as a binary counter, counting the number of field pulses modulo two, with the high and low polarization representing 0 and 1. Moreover, the four-state switching

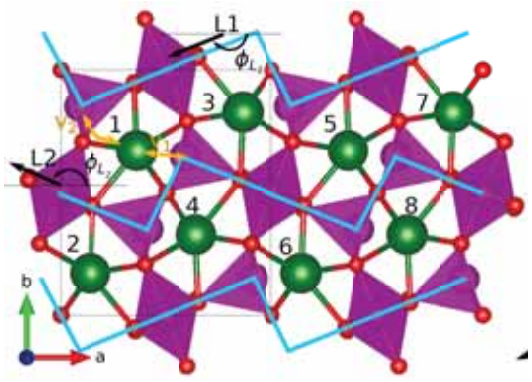

FIG. 1. **Magnetic unit cell of $GdMn_2O_5$.** Mn ions (purple spheres) form zig-zag chains (cyan lines) along the a-axis with antiferromagnetic intrachain interactions between Mn spins. $\mathbf{L}_1$ and $\mathbf{L}_2$ are the Néel vectors for the two distinct chains. Gd ions (green spheres) are inside pentagons formed by Mn ions from the neighboring chains. Red spheres are O ions, mediating superexchange interactions. The boundary of the structural unit cell is marked by the black box. The yellow arrows denote the exchange paths between Gd and the chains, that correspond to v_1 and v_2 in the model.

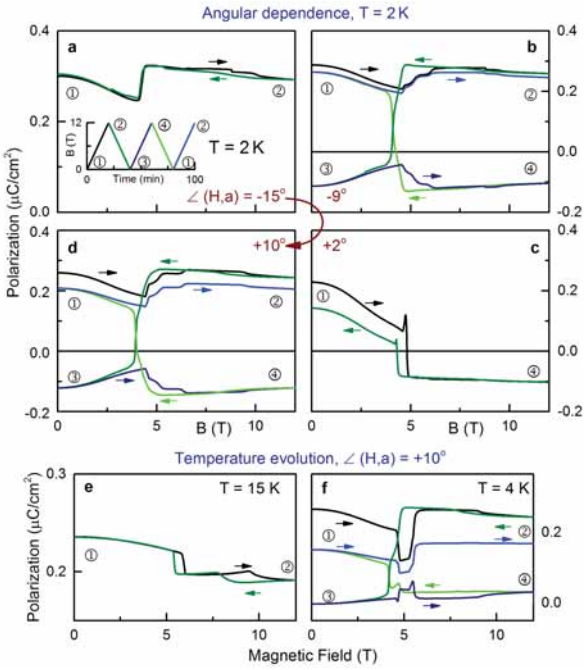

FIG. 2. **Evolution of the electric polarization loop across critical angle and critical temperature.** (a-d) Field dependence of the electric polarization of $GdMn_2O_5$ for different off-axis orientations of the applied magnetic field. (a,c): Conventional two-state switching is observed if magnetic field angle is (a) far larger than the "magic" direction or (c) very close to the crystallographic a-axis. (b,d): Unusual four-state hysteresis loop for the magnetic field direction close to the magic angle of $\pm 10°$. The inset shows the sequence of the magnetic field-sweeps. The labels 1-4 mark the four polarization states. The arrows show the direction of magnetic field-change during the sweep. The experiments have been done at $T = 2\,\mathrm{K}$. (e) At high temperatures only a small step is seen at the transition that shows some hysteresis and the two-state switching; (f) four-state switching starts to appear approximately beneath $T = 5$ K.

regime is found to be topologically distinct from, and protected by the existence of the two neighboring two-state switching regimes. It is characterized by a non-zero integer winding number, serving as a topological invariant [17].

$GdMn_2O_5$ has a centrosymmetric crystal lattice with Pbam (No. 55) space group symmetry [18]. Octahedrally coordinated Mn^{4+} ions and pyramidally coordinated Mn^{3+} ions form zigzag chains along the a-axis (cyan lines in Fig. 1) with antiferromagnetic (AFM) exchange interactions between neighbouring spins along the chains. Interchain exchange interactions are relatively weak and geometrically frustrated, as Mn ions from neighbouring chains form AFM pentagons [19–21].

$GdMn_2O_5$ orders magnetically at $T_{N1} = 40$ K, adopting an incommensurate state with the propagation vector $\mathbf{q} = (0.49, 0, 0.18)$. Below $T_{N2} = 33$ K it locks into a commensurate state with $\mathbf{q} = (1/2, 0, 0)$, showing one of the highest magnetically-induced electric polarizations of 3600 $\mu\mathrm{C/m}^2$, and a large variation (up to 5000 $\mu\mathrm{C/m}^2$) in an applied magnetic field [22]. This field-induced polarization variation is robust and changes very little when multiple field sweeps are applied. The electric polarization is induced by Heisenberg exchange striction on both Mn-Mn and Mn-Gd bonds, and has a large electronic component [23].

Experimental results – Figure 2 shows the evolution of the electric polarization in $GdMn_2O_5$ as a function of the external magnetic field. While in the previous studies only fields parallel to the a-axis were applied [22, 24], here we performed multiple experiments with the field tilted away from the a-axis in the ab plane by various angles, ϕ_H (see Fig. 2). This tilting has a dramatic effect on the ferroelectric polarization hysteresis curves. For temperatures above $\sim 5\,\mathrm{K}$, a field-induced reorientation transition is observed around 6 T which gives rise to a small hysteresis loop in agreement with previous results [22, 24] for $H \| a$. Below 5 K, and for fields around 5 T, an unusual hysteresis loop opens, as seen in Fig. 2(b,d,f). At low temperatures, this loop is characterized by a remarkable deterministic four-state cycle with polarization reversals, repeatable by applying further sweeps. The transition from state 1 to state 2 or from state 3 to state 4 upon increasing magnetic field does not change the electric polarization much. On the other hand, the decreasing magnetic field transforms state 2 into state 3, and state 4 into state 1, which results in the reversal of the electric polarization.

Systematic experiments with tilted magnetic fields show that the four-state sequence is not observed if the magnetic field is either close to the a-axis within $\pm 6°$ or is outside the $[-11°, +11°]$ interval, where only two of the four branches are cycled through, i.e. $1 \to 2$ or $1 \to 4$ (Fig. 2(a,c)) [22]. The novel magnetoelectric switching is observed around the two magic angles, $\pm\phi^*_\mathrm{H}$, with $\phi^*_\mathrm{H} \sim 10°$ (see Fig. 2(b,d)). Remarkably, the magic angle roughly matches the orientation [25, 26] of the Mn and Gd spins in zero field in one of the antiferromagnetic chains.

Modeling – In order to understand this puzzling behavior, we performed numerical simulations using a model of two interacting Mn chains (cyan lines in Fig. 1) and eight Gd spins per unit cell, coupled to external magnetic and electric fields. Due to the dominant AFM intrachain exchange interactions in RMn_2O_5 systems [21], neighboring Mn spins are assumed to remain largely antiparallel within each chain at all applied magnetic fields, and can thus be described by the two Néel vectors, $\mathbf{L}_\alpha$, where $\alpha = 1, 2$ labels the chain. $\mathbf{L}_\alpha$ are unit vectors, making the angles, ϕ_{L_α} with the a-axis, as shown in Fig. 1.

The Heisenberg exchange striction induces an electric polarization along the b-axis, with a contribution proportional to $\mathbf{L}_1 \cdot \mathbf{L}_2$, and a similar one originating from the Gd-Mn bonds. Since the Gd spin is relatively isotropic,

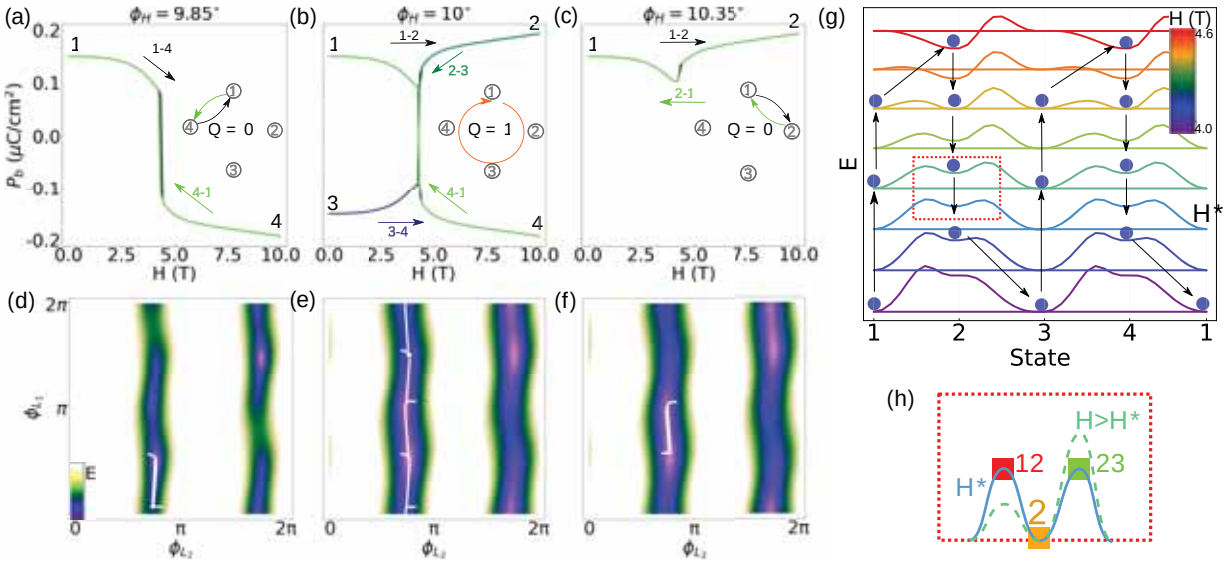

FIG. 3. **Simulation of magnetoelectric switching.** (a-c) Evolution of electric polarization P_b during the magnetic field sweep cycle for various magnetic field orientations. In each panel, the changes of the curve color indicate the same progression of the sweep cycle as Fig. 2. The four-state switching is seen for the field at the magic orientation. The insets indicate the corresponding switching paths and winding numbers. (d-f) Trajectories (in green) in the space of the Néel vectors orientations, (ϕ_{L_1}, ϕ_{L_2}), through the field sweep cycles in different regimes. The color map shows the energy landscape in the vicinity of the switching fields. (g) Evolution of transition barriers between states 1,2,3,4 as the magnetic field at 10° to the a axis is swept through the hysteresis region. The plots are shifted vertically, and color coded to distinguish the magnetic field strengths. Here the parameters were slightly altered to increase the width of the hysteresis region for illustrative purposes. The arrows and blue dots denote the trajectory of the energy minimum during the field sweep. Coordinated changes of the state energies and barrier asymmetry with magnetic field enable the topological behavior. (h) Schematic evolution of the barriers connecting the state 2 to states 1 and 3 in the vicinity of H^*. Saddle point states are denoted by 12 and 23.

it reorients easily to optimize the magnetic exchange energy, markedly increasing the contribution to the polarization through exchange striction as compared to other rare-earths [10, 22]. For further details on the effective Hamiltonian and the model parameters, see the discussion in the Methods section, following Eq. (1). The commensurate multiferroic state at zero field is fourfold degenerate as it breaks both time reversal symmetry, T: $(\mathbf{L}_1, \mathbf{L}_2) \rightarrow (-\mathbf{L}_1, -\mathbf{L}_2)$ and inversion symmetry, I, under which $(\mathbf{L}_1, \mathbf{L}_2) \rightarrow (-\mathbf{L}_1, +\mathbf{L}_2)$. States related by T have the same electric polarization, whereas states transforming into each other by I have polarizations of opposite sign.

The starting point of our simulations is one of the four degenerate ground states of the system in zero magnetic field. We track the (local) energy minimum through the energy landscape in the applied magnetic field, as its strength is ramped up and down. Field-induced transitions occur at spinodal points, at which a metastable state of the system becomes unstable.

The results of the simulations are shown in Fig. 3, where model parameters were chosen to reproduce the experimental hysteresis loop for the four-state switching as close as possible. This leads to a relatively narrow magic angle region, but, as discussed further in the Methods Section and, shown in Extended Data Fig. 1 and 2, the exact position and extent of the region can be tuned by changing the model parameters. The region itself is remarkably robust. Our model reproduces the experimentally observed four-state switching at the magic angle, $\phi_{\mathrm{H}}^* = 10°$, (Fig. 3(b)), and the switching between states 1 and 2 with close values of the electric polarization for $\phi_{\mathrm{H}} > \phi_{\mathrm{H}}^*$ (Fig. 3(c)).

We now turn to a more in-depth discussion of the peculiar four-state switching at the magic angle. The Mn and Gd spin configurations for the four states are shown in the red box in Fig. 4, and in greater detail in Extended Data Fig. 5. In the low-field states 1 and 3, Mn spins align close to the anisotropy axes of the two chains, with the Gd spins aligning generally antiparallel to the closest Mn spin, to which they are strongly coupled (v_1 in Fig. 1). This causes a roughly left-left-right-right sequence of the Gd spins. In the high-field states 2 and 4, Mn spins orient nearly orthogonal to the magnetic field due to the Zeeman interactions. The Gd spins are again influenced mostly by the AFM exchange with the nearest Mn ion, while being tilted slightly towards the external magnetic field. This tilting is one of the contributing factors to the peculiar unidirectional switching behavior, guiding the rotation of Mn spins. Figures 3(d-f) show the typical energy landscape in the $(\phi_{\mathrm{L1}}, \phi_{\mathrm{L2}})$-space calculated for three values of ϕ_{H}, at field magnitudes chosen to high-

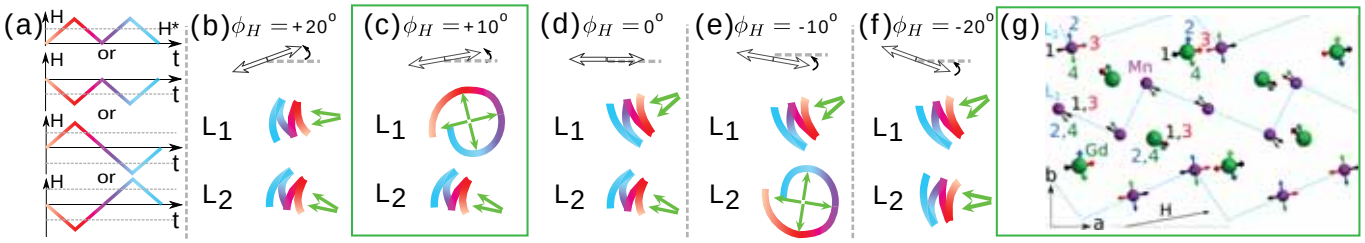

FIG. 4. **Magnetoelectric switching regimes.** (a) Time dependence of the magnetic field. The field is tilted by the angle ϕ_H away from the a axis. Color coding is used to indicate the synchronous evolution of the Néel order parameters, $\mathbf{L}_1$ and $\mathbf{L}_2$ in panels (b-f). For a fixed ϕ_H, each of the shown magnetic field ramp protocols (positive or negative field ramps) leads to the same result. (b) two-state switching for large positive ϕ: $\mathbf{L}_1$ and $\mathbf{L}_2$ toggle between two orientations. (c) four-state switching in the positive magic angle interval: $\mathbf{L}_1$ rotates, while $\mathbf{L}_2$ toggles, as shown in panel (g). (d) two-state switching at small ϕ_H: both order parameters toggle between two orientations. (e) four-state switching at the negative magic angle: $\mathbf{L}_1$ toggles, while $\mathbf{L}_2$ rotates in the direction opposite to that of $\mathbf{L}_1$ in panel (c). (f) two-state switching for a large negative ϕ_H: both order parameters toggle between two orientations. (g) spin configurations 1-4 in the magnetic unit cell, visited in the switching process at $\phi_H = 10°$.

light the differences between the three regimes. It consists of two narrow valleys elongated in the ϕ_{L_1}-direction and separated by the angle π in the ϕ_{L_2}-direction. These two valleys are time-reversal partners, and during the field sweeps the system remains inside one of them. This means that out of the total of eight states, four low-field states and four high-field states, only half is accessed during the field sweeps.

The approximate energy independence of the direction of $\mathbf{L}_1$ near the switching field is the result of the competition between the Zeeman and anisotropy energies of the Mn spins in chain 1, for which the magnetic field is tending towards the easy axis, as indicated by the black arrow in the red box of Fig. 4. This may also allow for a degree of electric control of the magnetic configuration, due to the coupling between the polarization and the soft magnetic mode [27]. A similar flattening of the energy surface occurs in textbook antiferromagnets near the spin-flop transition, where at a critical field applied along the easy axis, the spins flip perpendicular to the field in order to lower Zeeman energy by canting towards it. The important difference of the behavior discussed here is that the direction in which the spins progress during the up–and–down sweeps is unambiguous, i.e. the spins rotate unidirectionally throughout the cycling.

Another way to study the evolution of the system in different regimes is to compare the trajectories (white lines in Fig. 3(d-f)), describing the field-dependent state of the system. For all regimes, it is confined to a valley with ϕ_{L_1} varying much more than ϕ_{L_2}. In the topologically trivial regimes (Fig. 3(d,f)), the system remains in the neighbourhood of the starting point, with the trajectory contractible to a single point. In the four-state regime in Fig. 3(e), the system progresses through the entire valley unidirectionally, connecting the top and bottom edges, with $\mathbf{L}_1$ rotating a full 360°. This path cannot be contracted to a single point which highlights its *topologically distinct* nature as compared with the other two regimes. Indeed, one can define a winding number of a trajectory in the two-dimensional $(\phi_{\mathrm{L}1}, \phi_{\mathrm{L}2})$-space with a torus topology: $Q = \frac{1}{2\pi}\int_0^{t_0} dt(L_1^x \partial_t L_1^y - L_1^y \partial_t L_1^x)$, where the integral is taken over the time interval, t_0, during which the magnetic field is ramped up and down twice and the system returns to its initial state. In the two-state switching regime, $Q = 0$, whereas for the four-state switching, $Q = 1$. This means that as long as the two extremal regimes are present in the material (Fig 3 (d,f)), there will always exist a boundary region near the magic angle (Fig 3(e)), interpolating between the two, and leading to the circular four-state hysteresis. While the values of the model parameters decide the exact position and width of this topologically nontrivial region, we found that it is present for a surprisingly wide range of parameters, as shown in Fig. 1 and discussed further in the Methods section.

Focusing on the orientation of the Gd spins, we see that, as expected, they largely follow the chain they are most strongly coupled with; half of them undergoing a full-circle rotation, whereas the remaining half toggles back-and-forth together with $\mathbf{L}_2$. Thus, in the topological regime, the material mimics a crankshaft, transforming the back and forth changes of the external magnetic field ("the piston") into circular motions of the spins ("driveshaft").

To understand why the system follows the unidirectional trajectory in Fig. 3(e) when the field is oriented at the magic angle $\phi_{\mathrm{H}}^* = 10°$, we performed elastic string calculations of the barriers separating the different states, shown in Fig. 3(g). The simulation starts in the low-field state 1, which becomes metastable as the magnetic field increases. States 1 and 3 (2 and 4), related by spatial inversion that changes sign of $\mathbf{L}_1$, have equal energies, $E_1 = E_3$ ($E_2 = E_4$), for any applied magnetic field, in apparent contradiction with the unidirectional evolution, $1 \to 2 \to 3 \to 4$. The resolution of this paradox lies in

the fact that the energy barriers separating state 1 from states 2 and 4 are, in general, different, since the saddle-point states, 12 and 14 (see Fig. 3(h)), that determine the height of these barriers are not related by any symmetry transformation. Moreover, the evolution of these barriers in terms of the applied field is also asymmetric.

The top curve in Fig. 3(g) is calculated at the field H_1, at which state 1 becomes unstable and the barrier along the $1 \rightarrow 2$ path disappears, while the barrier separating states 1 and 4 is still present. On the downward field ramp, state 2 becomes unstable at $H = H_2$, when the barrier between states 2 and 3 vanishes while states 2 and 1 are still separated by a barrier (bottom curve), which leads to the $2 \rightarrow 3$ transition. When the magnetic field is increased and decreased again, the transition sequence $3 \rightarrow 4 \rightarrow 1$ occurs in precisely the same way: since the barrier states 34 and 12 (14 and 23) are related by inversion transformation, $E_{34} = E_{12}$ ($E_{41} = E_{23}$). The only difference is the opposite sign of the electric polarization. This evolution of the potential energy surface (discussed further in the Methods Section and in Extended Data Fig. 4) is equivalent to that of a Thouless charge pump, in particular, the one induced by circular motion in the two-dimensional parameter space of the Rice-Mele model [28] recently realized in ultracold gases [29–31].

The symmetries of the material relate the discussed switching regimes with others that are realized at different magnetic field angles. Figure 4 summarizes all of them, and a further discussion on this can be found in the Methods Section.

Outlook — The robust unidirectional spin rotation originates from the asymmetric evolution of the extremely flat energy landscape, which can be tuned by the angle and size of the applied external field. The behavior can be reproduced within a minimal model with a single AFM chain (Extended Data Fig. 3). This opens the door to the search and discovery of other such systems, by screening for those exhibiting two dissimilar neighboring switching regimes, thus ensuring the novel topological regime to be present as their boundary. The double hysteresis loop in $GdMn_2O_5$ turns it into an electric binary counter of magnetic field pulses, so that the ferroelectric polarization gives the number of pulses modulo 2. We hope this will inspire other electronic devices based on single crystal multiferroics. Finally, the flatness of the energy landscape leads to large variations of the order parameter in a narrow field strength window, making highly efficient switching conceivable.

[1] M. Bibes and A. Barthélémy, Towards a magnetoelectric memory, Nature Materials **7**, 425 (2008).

[2] W. Kleemann, Magnetoelectric spintronics, Journal of Applied Physics **114**, 027013 (2013).

[3] J. T. Heron, J. L. Bosse, Q. He, Y. Gao, M. Trassin, L. Ye, J. D. Clarkson, C. Wang, J. Liu, S. Salahuddin, D. C. Ralph, D. G. Schlom, J. Íñiguez, B. D. Huey, and R. Ramesh, Deterministic switching of ferromagnetism at room temperature using an electric field, Nature **516**, 370 (2014).

[4] F. Matsukura, Y. Tokura, and H. Ohno, Control of magnetism by electric fields, Nature Nanotechnology **10**, 209 (2015).

[5] S. Manipatruni, D. E. Nikonov, and I. A. Young, Beyond CMOS computing with spin and polarization, Nature Physics **14**, 338 (2018).

[6] S. Bhatti, R. Sbiaa, A. Hirohata, H. Ohno, S. Fukami, and S. N. Piramanayagam, Spintronics based random access memory: a review, Materials Today **20**, 530 (2017).

[7] A. I. Khan, A. Keshavarzi, and S. Datta, The future of ferroelectric field-effect transistor technology, Nature Electronics **3**, 588 (2020).

[8] Z. Zhang, Z. Wang, T. Shi, C. Bi, F. Rao, Y. Cai, Q. Liu, H. Wu, and P. Zhou, Memory materials and devices: From concept to application, InfoMat **2**, 261 (2020).

[9] N. A. Spaldin and R. Ramesh, Advances in magnetoelectric multiferroics, Nature Materials **18**, 203 (2019).

[10] D. Khomskii, Classifying multiferroics: Mechanisms and effects, Physics **2**, 20 (2009).

[11] M. Fiebig, Revival of the magnetoelectric effect, Journal of Physics D: Applied Physics **38**, R123 (2005).

[12] M. Fiebig, T. Lottermoser, D. Meier, and M. Trassin, The evolution of multiferroics, Nature Reviews Materials **1**, 16046 (2016).

[13] S.-W. Cheong and M. Mostovoy, Multiferroics: a magnetic twist for ferroelectricity, Nature Materials **6**, 13 (2007).

[14] J. F. Scott, Room-temperature multiferroic magnetoelectrics, NPG Asia Materials **5**, e72 (2013).

[15] Y. Tokunaga, N. Furukawa, H. Sakai, Y. Taguchi, T.-h. Arima, and Y. Tokura, Composite domain walls in a multiferroic perovskite ferrite, Nature Materials **8**, 558 (2009).

[16] Y. Tokunaga, Y. Taguchi, T.-h. Arima, and Y. Tokura, Electric-field-induced generation and reversal of ferromagnetic moment in ferrites, Nature Physics **8**, 838 (2012).

[17] D. Vanderbilt, *Berry Phases in Electronic Structure Theory: Electric Polarization, Orbital Magnetization and Topological Insulators* (Cambridge University Press, 2018).

[18] J. Alonso, M. Casais, M. Martínez-Lope, and M. Fernández-Díaz, A structural study from neutron diffraction data and magnetic properties of $R Mn_2O_5$ (R = La, rare earth), J. Phys. Cond. Mat. **9**, 8515 (1997).

[19] L. Chapon, G. Blake, M. Gutmann, S. Park, N. Hur, P. Radaelli, and S.-W. Cheong, Structural anomalies and multiferroic behavior in magnetically frustrated $TbMn_2O_5$, Phys. Rev. Lett. **93**, 177402 (2004).

[20] L. Chapon, P. Radaelli, G. Blake, S. Park, and S. Cheong, Ferroelectricity induced by acentric spin-density waves in YMn_2O_5, Phys. Rev. Lett. **96**, 097601 (2006).

[21] J.-H. Kim, M. A. van der Vegte, A. Scaramucci, S. Artyukhin, J.-H. Chung, S. Park, S.-W. Cheong, M. Mostovoy, and S.-H. Lee, Magnetic excitations in the low-temperature ferroelectric phase of multiferroic YMn_2O_5 using inelastic neutron scattering, Phys. Rev.

Lett. **107**, 097401 (2011).
[22] N. Lee, C. Vecchini, Y. Choi, L. Chapon, A. Bombardi, P. Radaelli, and S.-W. Cheong, Giant tunability of ferroelectric polarization in $GdMn_2O_5$, Phys. Rev. Lett. **110**, 137203 (2013).
[23] G. Giovannetti and J. van den Brink, Electronic correlations decimate the ferroelectric polarization of multiferroic $HoMn_2O_5$, Phys. Rev. Lett. **100**, 227603 (2008).
[24] S. H. Bukhari, T. Kain, M. Schiebl, A. Shuvaev, A. Pimenov, A. M. Kuzmenko, X. Wang, S.-W. Cheong, J. Ahmad, and A. Pimenov, Magnetoelectric phase diagrams of multiferroic $GdMn_2O_5$, Phys. Rev. B **94**, 174446 (2016).
[25] A. Munõz, J. Alonso, M. Casais, M. Martínez-Lope, J. Martínez, and M. Fernandez-Díaz, Magnetic structure and properties of $BiMn_2O_5$: A neutron diffraction study, Phys. Rev. B **65**, 144423 (2002).
[26] C. Vecchini, L. Chapon, P. Brown, T. Chatterji, S. Park, S.-W. Cheong, and P. Radaelli, Commensurate magnetic structures of RMn_2O_5 (R = Y, Ho, Bi) determined by single-crystal neutron diffraction, Phys. Rev. B **77**, 134434 (2008).
[27] Y. S. Oh, S. Artyukhin, J. J. Yang, V. Zapf, J. W. Kim, D. Vanderbilt, and S.-W. Cheong, Non-hysteretic colossal magnetoelectricity in a collinear antiferromagnet, Nature Communications **5**, 3201 (2014).
[28] M. J. Rice and E. J. Mele, Elementary excitations of a linearly conjugated diatomic polymer, Phys. Rev. Lett. **49**, 1455 (1982).
[29] M. Lohse, C. Schweizer, O. Zilberberg, M. Aidelsburger, and I. Bloch, A thouless quantum pump with ultracold bosonic atoms in an optical superlattice, Nature Physics **12**, 350 (2016).
[30] S. Nakajima, T. Tomita, S. Taie, T. Ichinose, H. Ozawa, L. Wang, M. Troyer, and Y. Takahashi, Topological thouless pumping of ultracold fermions, Nature Physics **12**, 296 (2016).
[31] M. Atala, M. Aidelsburger, J. T. Barreiro, D. Abanin, T. Kitagawa, E. Demler, and I. Bloch, Direct measurement of the Zak phase in topological Bloch bands, Nature Physics **9**, 795 (2013).
[32] A. Sushkov, M. Mostovoy, R. Valdés Aguilar, S.-W. Cheong, and H. Drew, Electromagnons in multiferroic RMn_2O_5 compounds and their microscopic origin, J. Phys. Cond. Mat. **20**, 434210 (2008).
[33] W. E, W. Ren, and E. Vanden-Eijnden, String method for the study of rare events, Phys. Rev. B **66**, 052301 (2002).
[34] G. Mills, H. Jónsson, and G. K. Schenter, Reversible work transition state theory: application to dissociative adsorption of hydrogen, Surface Science **324**, 305 (1995).
[35] The term due to the shift of the saddle point position along the reaction coordinate drops due to Hellmann-Feynman theorem.

Methods

Experimental Single crystals of $GdMn_2O_5$ were grown by flux method [22] and extensively characterized by X-ray analysis and by electric, dielectric, and magnetic measurements. From these experiments the magnetoelectric phase diagram in external magnetic fields was obtained [24]. Static electric polarization was measured on a small crystals of typical size $0.4 \times 0.4 \times 0.4\,\mathrm{mm}^3$ and using silver paste for electric contacts. The polarization was measured using an Keithley electrometer adapted to a Physical Property Measuring System, with magnetic fields of up to 14 T and temperatures down to 2 K. By changing the orientation of the sample in the cryostat, the direction of the magnetic field relative to the crystal axes was adjusted. We determined the crystal orientation using Laue analysis (accuracy $\sim$ 1 degree), transferred the sample to the cryostat, leading to a final uncertainty < 2 degrees, and performed the tilted field measurements in the range $[-20°, 20°]$ in steps of 2 degrees. In order to reduce the mechanical torque due to the off-axis magnetic field, the maximum field values were limited to 12 T.

Modeling

We now give a detailed description of the model that was used to reproduce the observed behavior. As was discussed in the main text, the state is characterized by two main sets of order parameters, $\mathbf{S}_i, i = 1...8$ for the Gd spins, and unit vectors $L_\alpha, \alpha = 1, 2$ for the AFM order parameters of the two inequivalent chains, inside the magnetic unit cell. We neglect quantum effects for large Gd f-spins (nominally $S = 7/2$). The spins interact with the external magnetic field, and induce the electric polarization P_b through the Heisenberg exchange striction. Thus we arrive at the Hamiltonian density (energy per magnetic unit cell):

$$
\begin{aligned}
H = \gamma(\mathbf{L}_1 \cdot \mathbf{L}_2)^2 + \sum_\alpha \chi((\mathbf{H} \cdot \mathbf{L}_\alpha)^2 - H^2) \\
- K_L \sum_\alpha (\mathbf{L}_\alpha \cdot \mathbf{n}_\alpha)^2 - \sum_i \left(K_S (\mathbf{N}_i \cdot \mathbf{S}_i)^2 + g\mu_\mathrm{B} \mathbf{H} \cdot \mathbf{S}_i \right) \\
+ \frac{1}{2}(g\mu_B)^2 \sum_{i \neq j} \left(\frac{\mathbf{S}_i \cdot \mathbf{S}_j}{r_{ij}^3} - 3\frac{(\mathbf{S}_i \cdot \mathbf{r}_{ij})(\mathbf{S}_j \cdot \mathbf{r}_{ij})}{r_{ij}^5} \right) \\
+ \sum_{i,\alpha} V_{i\alpha} \mathbf{S}_i \cdot \mathbf{L}_\alpha \\
- P_b[8\beta_1(\mathbf{L}_1 \cdot \mathbf{L}_2) + (\mathbf{S}_1 - \mathbf{S}_5)(\beta_2 \mathbf{L}_2 + \beta_3 \mathbf{L}_1) \\
+ (\mathbf{S}_2 - \mathbf{S}_6)(\beta_2 \mathbf{L}_1 + \beta_3 \mathbf{L}_2) + (\mathbf{S}_3 - \mathbf{S}_7)(\beta_2 \mathbf{L}_2 - \beta_3 \mathbf{L}_1) \\
+ (\mathbf{S}_4 - \mathbf{S}_8)(\beta_2 \mathbf{L}_1 - \beta_3 \mathbf{L}_2)] + P_b^2/2. \quad (1)
\end{aligned}
$$

The first term originates from the competition of the interchain exchange $J_\perp$ and the intrachain AFM exchange $J_\parallel$ [32], with $\gamma \sim \frac{J_\perp^2}{J_\parallel} > 0$. It describes the energy lowering due to spin canting, possible when $\mathbf{L}_1$ and $\mathbf{L}_2$ are non-collinear. The second term represents the Zeeman energy of the antiferromagnetically ordered Mn spins canted by the field; K_L and K_S are easy-axis anisotropy constants of Mn and Gd spins, and $\mathbf{n}_\alpha, \mathbf{N}_i$ are unit vectors along the easy axes, respectively. The third line describes the dipole-dipole interactions between Gd spins, which were restricted to five nearest neighbors. We verified that including further neighbors up to 8.5 Å within the ab-plane or neighbors along the c direction at 6.5 Å does not change the results qualitatively. The Heisenberg exchange constants $V_{i\alpha}$ describe Mn-Gd interactions, where $V_{i\alpha} = v_1$ for the exchange constant between the Gd and the Mn chain, containing the nearest (pentahedrally coordinated) Mn ion, and v_2 – the exchange coupling to the other Mn chain. The terms with $\beta_{1,2,3}$ describe the magnetoelectric interactions between P_b and $\mathbf{L}_\alpha$, $\mathbf{S}_i$, the last term being the dielectric energy. The model parameters chosen to fit the experimental data, and used in Fig. 3 of the main text, are $\gamma = 0.05$ meV, $\chi = 0.01$ meV^{-1}, $K_L = 1.1$ meV, $K_S = 0.09$ meV, $v_1 = 7.9$ meV, $v_2 = 0.15$ meV. The easy axes $\mathbf{n}_\alpha$ are aligned with the long segments of zigzag Mn chains (shown in blue in Fig. 1 of the main text) at $\pm 23.4°$ to the a-axis; $\mathbf{N}_i$ are at $\pm 12°$ to the a-axis in Extended Data Fig. 4(a). The exchange striction parameters were chosen to reproduce the size of hysteresis loops: $\beta_1 = 0.06\,\mu\mathrm{C/cm}^2$, $\beta_2 = 0.06\,\mu\mathrm{C/cm}^2$, $\beta_3 = 0.04\,\mu\mathrm{C/cm}^2$.

Since our model is phenomenological and not microscopic, and involves $\mathbf{L}_\alpha$ and $\mathbf{S}_i$ rather than all microscopic degrees of freedom, a trade-off aimed at minimizing the model complexity, the model parameters thus do not directly relate to microscopic interactions. This makes it very hard, if not impossible, to determine the exact values from ab-initio simulations. To determine the parameters, we started from a physically inspired initial guess, with the order of magnitude estimate for Mn-Mn exchange (inverse susceptibility χ^{-1}) from the ordering temperature, much smaller Gd-Mn exchange constants $v_1 > v_2$, an isotropic valence configuration of the Gd spins (d^7) suggesting low single-ion anisotropy K_S. Magnetostriction constants β_1,β_2 and β_3 were estimated from the height of hysteresis loops. We then proceeded to fine-tune the parameters in order to describe the experimental results as closely as possible.

We have used a string method to compute the transition pathways and barriers between the states, shown in Fig. 3(g) of the main text. Since the potential adopts the shape of an almost straight gutter, the string and nudged elastic band methods give comparable results [33, 34].

Using the definition of the winding number $Q = \frac{1}{2\pi} \int_0^{t_0} dt (L_1^x \partial_t L_1^y - L_1^y \partial_t L_1^x)$, we can study the influence that a variation of the model parameters has on the width and position of the "magic angle" region. The result is shown in Fig. 1. It is clear that a wide range of model parameters results in the existence of the topologically protected four-state switching regime. As discussed in the main text, as soon as the high and low angle regimes exist, there will be a boundary angle region where they cross over, leading to the four state switching. The ex-

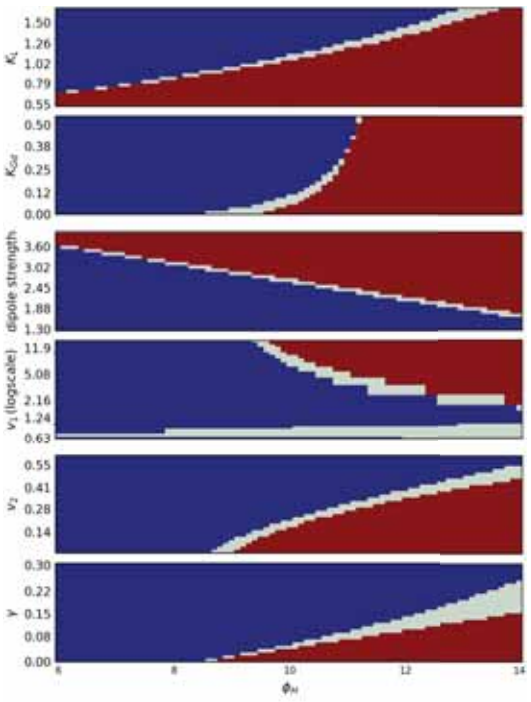

Extended Data Figure 1. **Magic Angle region.** The panels demonstrate the influence of selected model parameters on the magic angle region. In each panel only the parameter labeled on the vertical axis is varied, whereas the others are kept at the values reported in the text of this section, and used for Fig. 3 of the main text. All parameters are reported in units of meV. The blue regions signify the low angle switching regime, while the red denotes the high angle switching regime. The white boundary region is where the double loop switching regime occurs, characterized by a winding number of 1, and is topologically protected by the neighboring regimes.

act position and size depend on the details of the model parameters. Even more possibilities open up when more than one model parameter is varied. This leads us to believe that this behavior could be found in other materials.

We also observe that some parameters have a very strong effect on the four-state switching. For instance, taking $v_1 = 0.7$ dramatically increases the width of the four-state switching region to the interval of $[5.2°, 17.6°]$. However, even at much higher values of v_1, the four-state switching is maintained. A small variation of K_L, the strength of the Mn anisotropy, on the other hand, leads to large changes in the topologically protected region. This is not surprising, since the behavior of the Mn chains is very similar to that of the usual spin-flop transition, which crucially depends on the easy-axis anisotropy.

This adaptability of the model also allows us to use different parameters to increase the width of the hysteresis loop itself, in order to get a more detailed view of the switching trajectory of the system. Using the modified model parameters $v_1 = 3.33$ meV, $v_2 = 0.147$ meV, $K_L = 5.27$ meV, $\Gamma = 0.13$ meV, $K_{Gd} = 0.2$ meV, $\chi_L = 0.075$ meV and magnetodipolar interactions enhanced by a factor of 5.32, we find the energy surfaces as shown in Extended Data Fig. 2(d-f), demonstrating a more pronounced barrier asymmetry. The corresponding polarization loops and switching trajectories are also shown. Additionally, we were able to find a set of parameters with no anisotropy on Gd, or without dipolar interactions, that still gives rise to the crankshaft effect.

Combined with the results displayed in Fig. 3(g) of the main text, we can posit the barriers as the main determining factor for the described behavior. If one of the two extreme angle behaviors (high, and low angle) ceases to exist, or is never present in the first place, the boundary region (magic angle region) will also not be present. In the language of the energy surface, the effect ceases to exist when the lowest barrier between low and high field configurations does not change for any angle. E.g. the barrier between state 1 and state 4 is so much lower than the one between states 1 and 2, that no matter what the direction of the field is, the system will only toggle between states 1 and 4. One example would be that the anisotropy of the Gd spin is so high that it never orients towards the applied field, for feasible field strengths.

To further clarify the origin of the barrier asymmetry, we consider the system in state 2 at field H^*, at which the barriers, separating it from states 1 and 3, are equal $E_{12} = E_{23} = E_{34} = E_{41}$ (curve labelled with H^* in Fig. 3(h) of the main text). For a field H in the vicinity of H_*, $E_{23}(H) - E_{12}(H) \approx (H - H_*)(M_{12} - M_{23})$, where M_{12} and M_{23} are the magnetizations of the corresponding saddle point states at $H = H_*$ and $M_{23} > M_{12}$.

The contributions to the magnetization difference for every spin are shown in Extended Data Fig. 4(c) of the Methods section [35]. For $H > H_*$, $E_{12}(H) < E_{23}(H)$ and the barrier 12 disappears when the magnetic field increases, resulting in the $1 \to 2$ transition. For $H < H_*$, the barrier 23 is lower than 12 and disappears, triggering the $2 \to 3$ transition (see Fig. 3(h) of the main text).

The switching behaviour for $\phi_{\rm H} < 0$ follows from $\tilde{2}_x$ crystal symmetry combined with the translation by a, S_a, under which $(L_1^x, L_1^y) \to (L_2^x, -L_2^y)$. In this case, horizontal valleys appear in the potential energy landscape instead of the vertical ones cf. Fig. 3(d-f). Accordingly, $\mathbf{L}_2$ at the negative magic angle, $\phi_{\rm H} = -10°$, rotates in the direction opposite to the rotation direction of $\mathbf{L}_1$ at $\phi_{\rm H} = +10°$. The rotation direction is unchanged under the magnetic field reversal ($\mathbf{L}_{1,2}$ is invariant under T combined with S_a, whereas $\mathbf{H}$ changes sign), and under the combined reversal of $\mathbf{L}_1$ and $\mathbf{L}_2$. Hence, no antiferromagnetic domain selection by magnetoelectric cooling is required for the unidirectional circular switching of spins, and all protocols shown in Fig. 4(a) of the main text lead to the same result. At $\phi_{\rm H} = \pm 20°$, both Néel vectors toggle between two directions in such a way that the angle between them and, hence, the electric polar-

ization changes very little, as indicated in Fig. 4(b,f) of the main text. On the other hand, at $\phi_{\rm H} = 0°$, $\mathbf{L}_1$ and $\mathbf{L}_2$ tilt in opposite directions. The resulting large variation of the angle between these two vectors gives rise to the two-state switching with the polarization reversal, as seen in Fig. 4(d) of the main text. This suggests that small-amplitude relative rotation of $\mathbf{L}_1$ and $\mathbf{L}_2$ is an electromagnon mode that could be excited by oscillating H_a or E_b. The full-circle rotation of $\mathbf{L}_1$ occurs in the crossover region between the two toggling regimes, as shown in Fig. 4(c,e) of the main text.

To clarify the relative importance of various interactions for the four-state switching, their contributions are plotted in Extended Data Fig. 4(b) of the Methods section, with accompanying discussion.

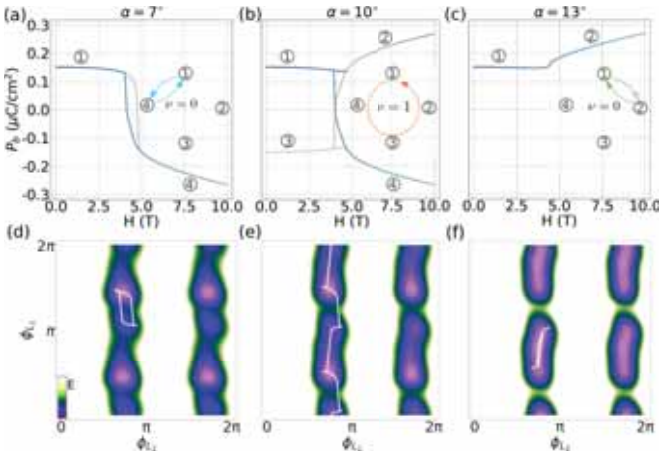

Extended Data Figure 2. **Switching with modified model parameters.** (a-c) Evolution of electric polarization P_b during the magnetic field sweep cycle for various magnetic field orientations. In each panel, the changes of the curve color from red to blue indicate the progression of the sweep cycle. The four-state switching is seen for the field at the magic orientation. The insets indicate the corresponding switching paths and winding numbers. (d-f) Trajectories (in white) of AFM order parameter orientations $(\phi_{\rm L_1}, \phi_{\rm L_2})$ through the field sweep cycles in different regimes. The color map shows the energy landscape at an intermediate field H^*.

Having modelled the topologically protected switching in $GdMn_2O_5$ with all its complexity, one may wonder what the minimal requirements are to have a similar behavior where spins make a full 360° rotate when the applied field, while oscillating in magnitude, always points in one direction. As seen in Fig. 3 of the main text, spins in the chain most parallel to the applied field perform the full rotation, while those in another chain merely toggle around their initial orientation. Gd moments mostly follow the behavior of the chain they are most strongly coupled to. This warrants an attempt to explain the observed behavior using only a single Mn chain, with Gd spins, coupled to it via v_1. In the particular case where the magic angle is along $\phi_H = +10°$, we keep L_1, S_2,

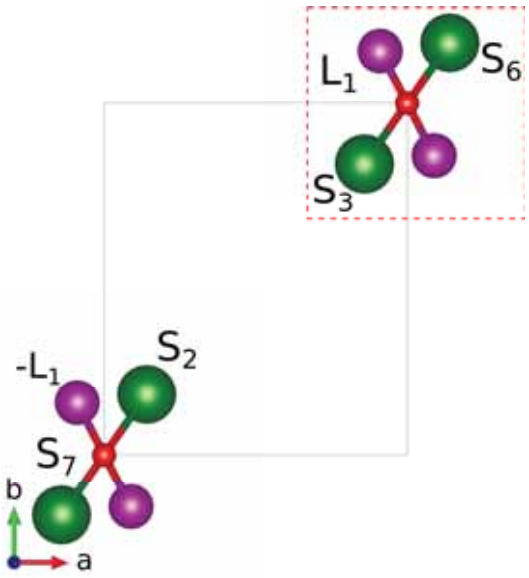

Extended Data Figure 3. **Simplified single chain model.** The crankshaft behavior can be reproduced within the model that only involves the single AFM chain (purple ions), coupled to Gd ions $\mathbf{S}_3$ and $\mathbf{S}_6$ (indicated by the dashed rectangle).

S_3, S_6 and S_7 as the variables in the model. We also neglect the easy axis anisotropy of Gd spins. This leaves us with the following Hamiltonian, combining two parts, one with the dipolar terms H_{dip} and another with all the other terms H':

$$\begin{aligned} H &= H' + H_{dip} \\ H' &= v_1(\mathbf{S}_2 + \mathbf{S}_3 - (\mathbf{S}_6 + \mathbf{S}_7)) \cdot \mathbf{L}_1 \\ &\quad - g\mu_b(\mathbf{S}_2 + \mathbf{S}_3 + \mathbf{S}_6 + \mathbf{S}_7) \cdot \mathbf{H} \\ &\quad + K_L(\mathbf{L}_1 \cdot \mathbf{n})^2 \\ H_{dip} &= \frac{1}{2}(g\mu_B)^2 \sum_{i \neq j} \left(\frac{\mathbf{S}_i \cdot \mathbf{S}_j}{r_{ij}^3} - 3\frac{(\mathbf{S}_i \cdot \mathbf{r}_{ij})(\mathbf{S}_j \cdot \mathbf{r}_{ij})}{r_{ij}^5} \right). \end{aligned} \tag{2}$$

Using the symmetry, we set S2 = S3 and S6 = S7 (see Extended Data Fig. 3), and, keeping only the nearest-neighbor magnetodipolar terms, we arrive to

$$\begin{aligned} H' &= 2v_1(\mathbf{S}_3 - \mathbf{S}_6) \cdot \mathbf{L}_1 - 2g\mu_b(\mathbf{S}_3 + \mathbf{S}_6) \cdot \mathbf{H} \\ &\quad + K_L(\mathbf{L}_1 \cdot \mathbf{n})^2 \\ H_{dip} &= (g\mu_B)^2 \left(\frac{\mathbf{S}_3 \cdot \mathbf{S}_6}{r_{36}^3} - 3\frac{(\mathbf{S}_3 \cdot \mathbf{r}_{36})(\mathbf{S}_6 \cdot \mathbf{r}_{36})}{r_{36}^5} \right), \end{aligned} \tag{3}$$

as a minimal model that still demonstrates the crankshaft-like behavior.

Turning to the evolution of the energy contributions during the field sweeps, shown in Extended Data Fig. 4, we can observe that, although the transitions between the low-field states, 1 and 3, and the high-field states, 2 and 4, have the appearance of spin-flop transition in the Mn magnetic subsystem, the largest energy decrease in the

high-field states is associated with the Zeeman energy of Gd spins, which comes mostly at the expense of the Gd-Mn exchange energy. The energy of Mn spins actually increases at the transition to the high-field state, whereas at the Mn spin-flop transition the opposite should occur. Artificially changing the strength of dipole-dipole interactions leads to a shift of the magic angle region, as shown in Extended Data Fig. 1.

DATA AVAILABILITY STATEMENT

The data that support the findings of this study are available via:
https://doi.org/10.5281/zenodo.5817751

CODE AVAILABILITY

The code of the model used to produce the fits is available on GitHub:
`https://github.com/louisponet/GdMn2O5_paper`.

ACKNOWLEDGMENTS

This work was supported by the Austrian Science Funds (I 2816-N27, P 32404-N27). The work at Rutgers University was supported by the DOE under Grant No. DOE: DE-FG02-07ER46382. MM acknowledges Vrije FOM-programma 'Skyrmionics'.

COMPETING INTERESTS

The authors declare no competing interests.

AUTHOR CONTRIBUTION

A.P. initiated the project; A.P., S.A., M.M. and S.W.C, supervised the project; A.S. and T.K. designed the experiment; X.W. grew the samples; Ann.P., T.K., and J.W., characterized the samples using various techniques; J.W. and T.K. conducted the experiments and analyzed the data; L.P., S.A., and M.M. developed the theory; L.P., S.A., A.P., and M.M. wrote the manuscript with the feedback from all authors.

ADDITIONAL INFORMATION

Corresponding author Correspondence to S. Artyukhin.

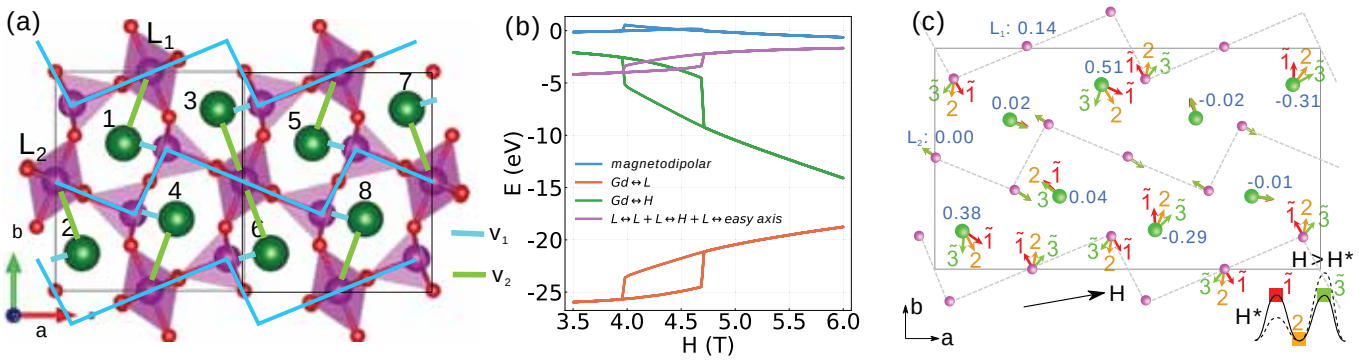

Extended Data Figure 4. (a) Exchange interactions between Gd ions and neighboring AFM Mn chains ($v_{1,2}$). Easy axes for $L_{1,2}$ coincide with the longer zigzag segments; for Gd – with blue lines indicating v_1 exchange. (b) Field dependence of energy contributions: magnetodipolar interactions, Gd-Mn exchange, Zeeman energy of Gd spins and energy of AFMally ordered Mn spins, for the field pointing at 10° to the a axis. (c) Spin configuration in state 2 and in the states, corresponding to the saddle points at the barriers toward the neighboring minima at $H = H^*$ (states and color coding for spins is indicated in the inset). The numbers in blue show the field projections of magnetization difference of Gd and Mn ions in the saddle point states. The difference of magnetization components along the field in two saddle point states results in the asymmetric barrier evolution when the field is varied.

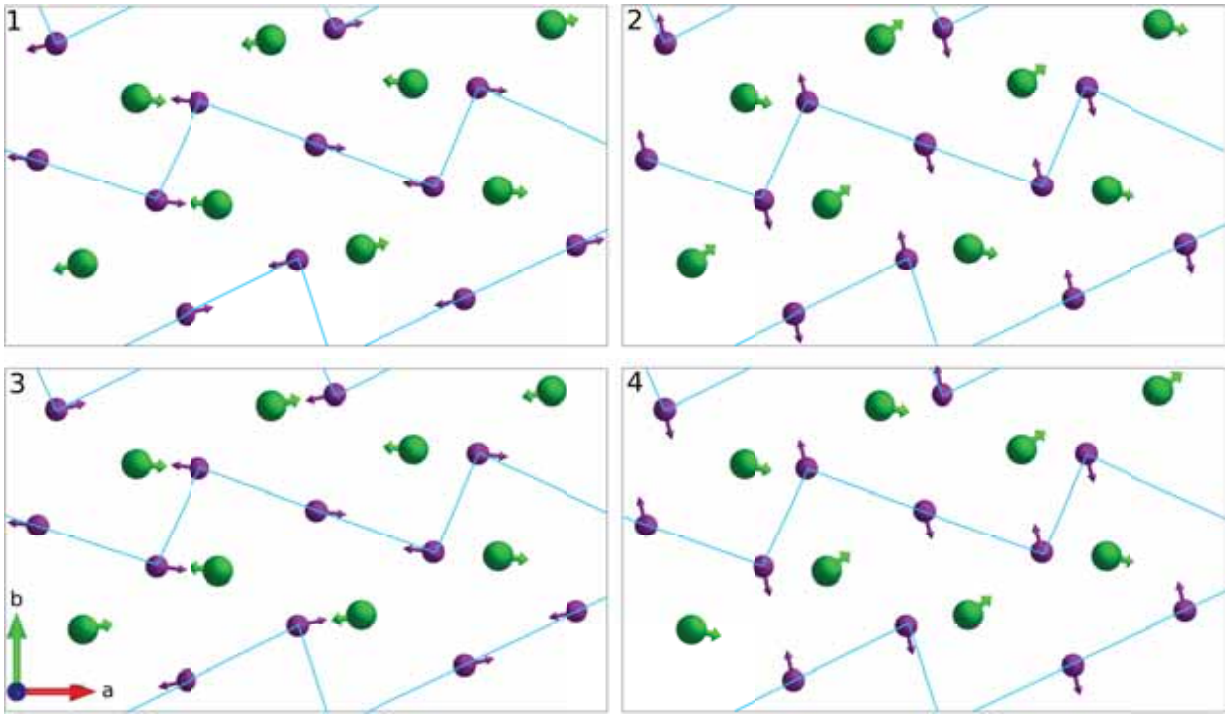

Extended Data Figure 5. The spin configurations corresponding to the four states. Gd ions are shown in green while Mn ions are in purple. The blue lines indicate the antiferromagnetic zigzag chains.